Structure-guided examination of the mechanogating mechanism of PIEZO2

Francisco J. Taberner[a,b,1], Vincenzo Prato[a,1], Irina Schaefer[a], Katrin Schrenk-Siemens[a], Paul A. Heppenstall[b], and Stefan G. Lechner[a,2]

[a]Institute of Pharmacology, Heidelberg University, 69120 Heidelberg, Germany; and [b]Cell Biology and Biophysics Unit, European Molecular Biology Laboratory, 00016 Monterotondo, Italy

Piezo channels are mechanically activated ion channels that confer mechanosensitivity to a variety of different cell types. Piezos oligomerize as propeller-shaped homotrimers that are thought to locally curve the membrane into spherical domes that project into the cell. While several studies have identified domains and amino acids that control important properties such as ion permeability and selectivity as well as inactivation kinetics and voltage sensitivity, only little is known about intraprotein interactions that govern mechanosensitivity—the most unique feature of PIEZOs. Here we used site-directed mutagenesis and patch-clamp recordings to investigate the mechanogating mechanism of PIEZO2. We demonstrate that charged amino acids at the interface between the beam domain—i.e., a long α-helix that protrudes from the intracellular side of the "propeller" blade toward the inner vestibule of the channel—and the C-terminal domain (CTD) as well as hydrophobic interactions between the highly conserved Y2807 of the CTD and pore-lining helices are required to ensure normal mechanosensitivity of PIEZO2. Moreover, single-channel recordings indicate that a previously unrecognized intrinsically disordered domain located adjacent to the beam acts as a cytosolic plug that limits ion permeation possibly by clogging the inner vestibule of both PIEZO1 and PIEZO2. Thus, we have identified several intraprotein domain interfaces that control the mechanical activation of PIEZO1 and PIEZO2 and which might thus serve as promising targets for drugs that modulate the mechanosensitivity of Piezo channels.

PIEZO2 | PIEZO1 | mechanotransduction | structure-function

PIEZO1 and PIEZO2 are mechanically activated ion channels that confer mechanosensitivity to a wide variety of cell types (1, 2). PIEZO1 mediates shear stress and stretch-induced transmembrane currents mainly in nonneuronal cells such as erythrocytes, vascular endothelial cells, bladder urothelial cells, and chondrocytes, whereas PIEZO2 is predominantly expressed in sensory neurons and is required for proprioception (3, 4), the detection of light touch (5–9), and the detection of noxious mechanical stimuli (10–12). Accordingly, mutations in PIEZO channels have been linked to numerous diseases including dehydrated hereditary stomatocytosis, congenital lymphatic dysplasia, and several arthrogryposis disorders (5, 13–18). Consistent with their different physiological roles, PIEZO1 and PIEZO2 also differ in their biophysical properties. Thus, PIEZO1 is sensitive to both pressure-induced membrane stretch and localized membrane deformation with a mechanical probe, whereas PIEZO2 is reliably activated only by the latter type of stimulus (1, 19–21). Moreover, PIEZO1-mediated currents inactivate significantly slower than PIEZO2 currents (22). However, despite significant progress in characterizing the biophysical properties and understanding the physiological roles of PIEZO channels, we still know only little about how they function at the molecular level.

Three recently published high-resolution cryo-electron microscopy (cryo-EM) studies revealed that PIEZO1 oligomerizes as a homotrimer that exhibits a propeller-shaped architecture (23–25). The propeller blades are thought to be formed by 36 transmembrane (TM) helices, but owing to the low resolution

of the cryo-EM maps in the periphery of the channel, only 24 of these TMs have been structurally resolved (23, 25). The ion conduction pathway of the PIEZO1 trimer is lined by the three inner transmembrane helices (IHs) and by a short α-helix of the cytosolic C-terminal domain (CTD^{α3}) and has two narrow constrictions at its cytosolic neck. The upper constriction is formed by M2493 of the IH and the lower constriction by P2536 and E2537 of CTD^{α3}. On the extracellular side the ion conduction pathway possibly extends through the propeller cap, which is formed by the C-terminal extracellular domains (CEDs) that are connected to the IHs and the adjacent outer TM helices (OHs) via flexible linkers.

Several studies have identified amino acids that control ion permeability and selectivity, inactivation kinetics, and voltage sensitivity of PIEZO1 (14, 20, 26–30), but only little is known about how these properties are controlled in PIEZO2. Moreover, mechanosensitivity, which is the most fundamental and unique distinguishing feature of PIEZOs, is only poorly understood. Ligand- and voltage-gated ion channels open as a result of conformational changes induced by the binding of ligands or by movements of the voltage-sensing transmembrane helices, respectively. How mechanical stimuli induce conformational changes in the mechanically gated PIEZO channels to activate them is, however, unknown. One possible mechanism is that mechanical deformations of the cell are transmitted to PIEZOs via molecular tethers that connect the channel with the extracellular

Significance

Aristotle's five senses—sight, smell, taste, hearing, and touch—are crucial for the perception of and interaction with the environment. While the molecular machineries that detect visual, olfactory, gustatory, and auditory stimuli are well characterized, comparatively little is known about how the sense of touch works at the molecular level. Here we identified and characterized intraprotein domain interfaces that govern the mechanosensitivity of the ion channel PIEZO2. Considering that PIEZO2 is an important detector of tactile and painful mechanical stimuli, selectively blocking these domain interactions in primary afferent neurons might provide an effective means to modulate pain sensitivity. Thus our work provides the basis for the development of additional types of analgesics that attack pain at its source.

matrix and the cytoskeleton. While there is evidence suggesting that an extracellular tether might contribute to the activation of mechanotransduction currents in mouse low-threshold mechanoreceptors (31), which are mediated by PIEZO2 (7), the requirement of a tether seems unlikely for PIEZO1. In fact, there is experimental evidence suggesting that PIEZO1 is directly gated by "force-from-lipid" mechanisms, as it can be activated in cytoskeleton-deficient blebs (32) and, most importantly, in lipid bilayers that contain no other cellular components (33). Force-from-lipids might arise from a hydrophobic mismatch between hydrophobic transmembrane domains of PIEZOs and the hydrophobic portion of the membrane, which could result from membrane stretch-induced thinning of the membrane or from changes in the membrane curvature around the channel. Considering that PIEZO1 appears to curve the membrane locally into a spherical dome that projects into the cell, the latter mechanism seems more likely. Considering the architecture of PIEZO1, it has been speculated that the blade domains, which are formed by 36 of the overall 38 TM helices, play an important role in sensing membrane tension. Indeed, deleting the extracellular loops that connect TM15 with TM16 and TM19 with TM20 of the blade renders PIEZO1 insensitive to mechanical stimuli (23) and localized application of force to the blade domains using magnetic nanoparticles seems to stabilize the open conformation of PIEZO1 (34). Whether the blade domain has the same function in PIEZO2 is, however, completely unclear. It has further been speculated that conformational changes of the blades might be transmitted to the pore by the so-called beam domain—i.e., a long α-helix that protrudes from the intracellular side of the blade toward the inner vestibule of the channel—via a lever-like mechanism (23, 35). However, experimental evidence for such a lever-like mechanogating mechanism of PIEZO1 has not yet been provided.

Here we set out to identify intraprotein interactions that govern the mechanosensitivity PIEZO2 using site-directed mutagenesis and patch-clamp recordings.

Results

PIEZO2 Protein Structure Homology Modeling. To identify interdomain interactions that govern the mechanogating of PIEZO2, we modeled the tertiary and quaternary structure of PIEZO2, which has not yet been resolved, using the SWISS-MODEL protein structure homology-modeling server (36) and the PIEZO1 structure described by Guo and MacKinnon (25) as a template. PIEZO2 and PIEZO1 differ most notably in the amino acid (AA) sequence and size of several intrinsically disordered regions (IDRs) that connect, for example, the proximal end of the beam with the blade (IDR2 and IDR3) as well as different TMs of the blade domain (IDR1 and IDR4–6) (Fig. 1A). Since the structures of these cytosolic domains were not resolved in PIEZO1—most likely due to their intrinsically disordered nature—we did not consider them when modeling the structure of PIEZO2. However, in the domains for which the PIEZO1 structure has been resolved, PIEZO1 and PIEZO2 exhibit extremely high AA sequence similarity (Fig. 1A) and accordingly our homology model suggested that PIEZO2 has a very similar overall structure to PIEZO1 (Fig. 1B). The homology model further suggests that the upper and lower pore constrictions of PIEZO2 are formed by the highly conserved AAs M2767 and E2811, respectively.

Noncovalent Interactions Between the Beam and CTD Facilitate Mechanical Activation of PIEZO2. To gain insights into the mechanogating mechanism of PIEZO2, we first considered the role of the beam domain, which—in PIEZO1—had been proposed to act as a lever that allosterically couples possible conformational changes of the blade domains to the pore-forming domains (23, 35). To this end we generated PIEZO2 mutants in which putative beam–CTD interactions were disrupted by alanine substitution (M1491A/L1494A, R1500A/R1504A, D2783A, Y1508A/K1512A; Fig. 2A) and compared the mechanosensitivity of these mutant channels with PIEZO2 wild type (PIEZO2-WT). Mechanosensitivity of the PIEZO2 mutants was assessed in N2a-PIEZO1-KO cells, which do not exhibit any endogenous mechanically activated currents (20), using a refined version of the mechano-clamp
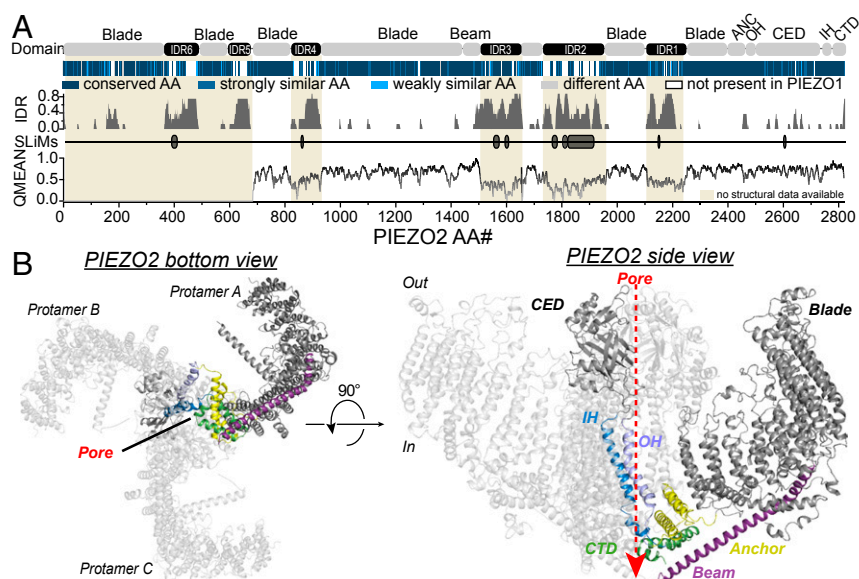
Fig. 1. PIEZO2 structure homology model. (A) Color-coded sequence alignment of the indicated domains of PIEZO2 and PIEZO1 (Top), prediction of intrinsically disordered regions (IDR) and short linear motifs (SLiMs) using IUPred (Middle), and local quality plot (QMEAN, Bottom) of the PIEZO2 structure homology model. Note that regions whose structure has not been resolved in PIEZO1 (beige shaded areas) and which are bigger in PIEZO2 (IDR2 and -5 are almost completely missing in PIEZO1 and IDR2, -4, and -6 are only half as big; see sequence alignment in Top) are predicted to be intrinsically disordered (Middle), and accordingly the local QMEANs (Bottom) are very low in these regions. (B) Bottom (Left) and side (Right) views of the modeled PIEZO2 trimer. Abbreviations: CED, C-terminal extracellular domain; CTD, C-terminal domain; IH, inner helix; OH, outer helix.

Fig. 2. Noncovalent interactions between the beam and the CTD facilitate mechanical activation of PIEZO2. (*A*) The beam domain has been proposed to act as a lever that rotates around a pivot constituted by the beam–CTD interface. *Bottom* shows a magnified view of the beam–CTD interface of PIEZO2 with the possible noncovalent interactions being depicted by dashed lines. (*B*) Example traces of mechanically activated currents evoked by increasing mechanical stimuli (*Top*) mediated by the indicated PIEZO2 mutants in N2a-P1KO cells. Note that D2783A and R1500A/R1504A mutants generate much smaller currents that PIEZO2-WT. (*C*) Displacement–response curves (mean ± SEM peak current amplitudes) of the indicated PIEZO2 mutants. *N* numbers are shown in the graph. (*D*) Example traces of PIEZO2-WT currents (*Left*) and D2783A currents (*Right*) are shown to illustrate how the mechanical thresholds that are compared in *E* were determined and how the inactivation time constants shown in *F* were determined by fitting the currents with a single exponential equation. (*E*) Comparison of the mean ± SEM activation thresholds of the mechanically activated currents mediated by the indicated channel mutants using one-way ANOVA with Dunnett's multiple-comparison test. ****$P < 0.0001$. (*F*) Comparison of the mean ± SEM inactivation time constants (τ_{inact}) using one-way ANOVA with Dunnett's multiple-comparison test. (*G*) Superimposed example traces (gray) of currents from the indicated mutants evoked by 100 consecutive and identical mechanical stimuli. The thick black, green, and purple lines show the mean response waveforms obtained by averaging all currents. (*H–J*) The variance of the difference between the measured and the scaled mean waveform at each sampling point is plotted against the current amplitude of the mean scaled waveform in 1-pA bins and fitted using the equation $\sigma^2 = \sigma_0^2 + iI - I^2/N$, where i is the single-channel current (see *Materials and Methods* and *SI Appendix*, Fig. S3 for details). (*K*) Comparison of the mean single-channel currents ± SEM.

technique (*SI Appendix*, Fig. S1) that allows a more accurate determination of the apparent mechanical threshold of PIEZO2 than the classical mechano-clamp technique (37–39). These recordings indicated that D2783 and R1500/R1504 are involved in the mechanical activation of PIEZO2, because both mutants (D2783A and R1500A/R1504A) exhibited significantly higher mechanical thresholds (D2783A, 2.64 ± 0.11 μm; R1500A/R1504A, 2.27 ± 0.14 μm vs. PIEZO2, 1.52 ± 0.10 μm) and generated smaller mechanically activated currents, while the M1491A/L1494A- and the Y1508A/K1512A-mediated currents were indistinguishable from PIEZO2-WT currents (Fig. 2 *B–E*). The inactivation kinetics were not altered in any of the mutants (Fig. 2*F*).

A limitation of the mechano-clamp technique is that large mechanical stimuli (>5 μm in N2a cells) frequently led to gigaseal instability or destruction of the cell, which precludes measurements of the maximal current amplitudes of mutants with high mechanical thresholds. We thus next investigated whether the reduced current amplitudes of the D2783A and R1500A/R1504A mutants are solely the consequence of the increased

mechanical thresholds, which inevitably cause a right shift of the displacement response curve, or whether other factors also contribute. Immunocytochemistry and, most importantly, Western blot analysis showed that both mutants were present in the cell membrane at similar levels to PIEZO2 wild type, indicating that the reduced current amplitudes of these mutants do not result from deficits in channel expression or trafficking (*SI Appendix*, Fig. S2 *A–C*). Moreover, both mutants had similar reversal potentials to PIEZO2-WT (*SI Appendix*, Fig. S2 *D* and *E*) and did not exhibit altered velocity dependence of activation (*SI Appendix*, Fig. S2*F*). Finally, we also considered the possibility that the alanine substitutions—via an allosteric mechanism—might alter single-channel conductance. Unlike PIEZO1, PIEZO2 is mostly insensitive to pressure-induced membrane stretch, which precludes single-channel recordings of PIEZO2 (1, 19–21). Hence, to determine the single-channel current amplitude of PIEZO2 and the loss-of-function mutants, we utilized nonstationary noise analysis (NSNA). A comparison of the PIEZO1 unitary current amplitudes determined with NSNA of poking-evoked currents and single-channel recordings of pressure-evoked currents showed

Taberner et al.

that NSNA allows the precise determination of unitary current amplitudes from poking-evoked whole-cell currents (*SI Appendix*, Fig. S3). NSNA of PIEZO2-WT, D2783A, and R1500A/R1504A showed that all three channel variants have similar single-channel current amplitudes (PIEZO2, 3.56 ± 0.46 pA; D2783A, 4.64 ± 0.54 pA; R1500A/R1504A, 4.01 ± 0.71 pA; Fig. 2 *G–K*), which were slightly higher than the single-channel amplitude of PIEZO1.

Hence, in summary our data showed that substituting charged residues at the interface between the beam and the CTD by uncharged alanines significantly increases the mechanical threshold of PIEZO2, which results in a twofold reduction of PIEZO2 current amplitudes at any given stimulus magnitude, but does not affect other channel properties.

The Beam-To-Latch Linker Controls Ion Permeation of PIEZOs. We next examined whether the beam serves as a lever, as previously proposed (23, 35). To this end we completely removed the load arm of the putative lever from PIEZO2, by deleting the proximal end of the beam together with the latch and the intrinsically disordered region that connects the beam with the latch [beam-to-latch linker (B2L-linker)] that should be located underneath the channel pore (Fig. 3 *A* and *B*). Unexpectedly, rather than exhibiting reduced mechanosensitivity, the PIEZO2-B2L^{del} mutant channel had lower mechanical thresholds and generated significantly larger mechanically gated currents than PIEZO2-WT (Fig. 3 *C–E*). The mean inactivation time constant of PIEZO2-B2L^{del} currents (3.5 ± 0.26 ms) was slightly but not significantly bigger than that of PIEZO2-WT currents (2.86 ±

0.19 ms; Fig. 3*F*) and the reversal potentials of the two channels did not significantly differ from one another (PIEZO2-WT, 11.9 ± 1.2 mV, n = 7 vs. PIEZO2-B2L^{del}, 15.4 ± 3.2 mV, n = 5, Student's *t* test, P = 0.268).

Considering its putative location, we hypothesized that the B2L-linker and/or the latch might serve as a cytosolic plug that limits ion permeation by blocking the exit of the ion conduction pathway formed by the CTD (i.e., the inner vestibule), which could explain why removing the B2L-linker/latch results in channels that produce larger currents. To test this hypothesis, we measured the single-channel current amplitudes of PIEZO2-B2L^{del}–mediated currents using nonstationary noise analysis. This analysis revealed that the PIEZO2-B2L^{del} mutant indeed has an almost two times greater single-channel current amplitude than PIEZO2-WT (Fig. 3 *G–I*), which is consistent with the difference in whole-cell current amplitudes (Fig. 3*D*).

Owing to the lack of structural information, reliable predictions about how the B2L-linker might interact with the inner vestibule of PIEZO2 to limit ion permeation are impossible. However, the latch domain, which is part of a larger hydrophobic stretch and the structure of which was resolved by Saotome *et al.* (24), could bind to the inner vestibule via hydrophobic interactions of Y1568/L1570/F1571 with F2805 and/or W2816 of the CTD (Fig. 3 *A* and *B*). To test this hypothesis, we generated a PIEZO2 triple mutant in which the latch presumably has a lower affinity to the CTD by substituting Y1568/L1570/F1571 with alanines (YLF→AAA). Similar to the B2L^{del} mutant, the YLF→AAA mutant produced larger currents than PIEZO2-WT. However, the
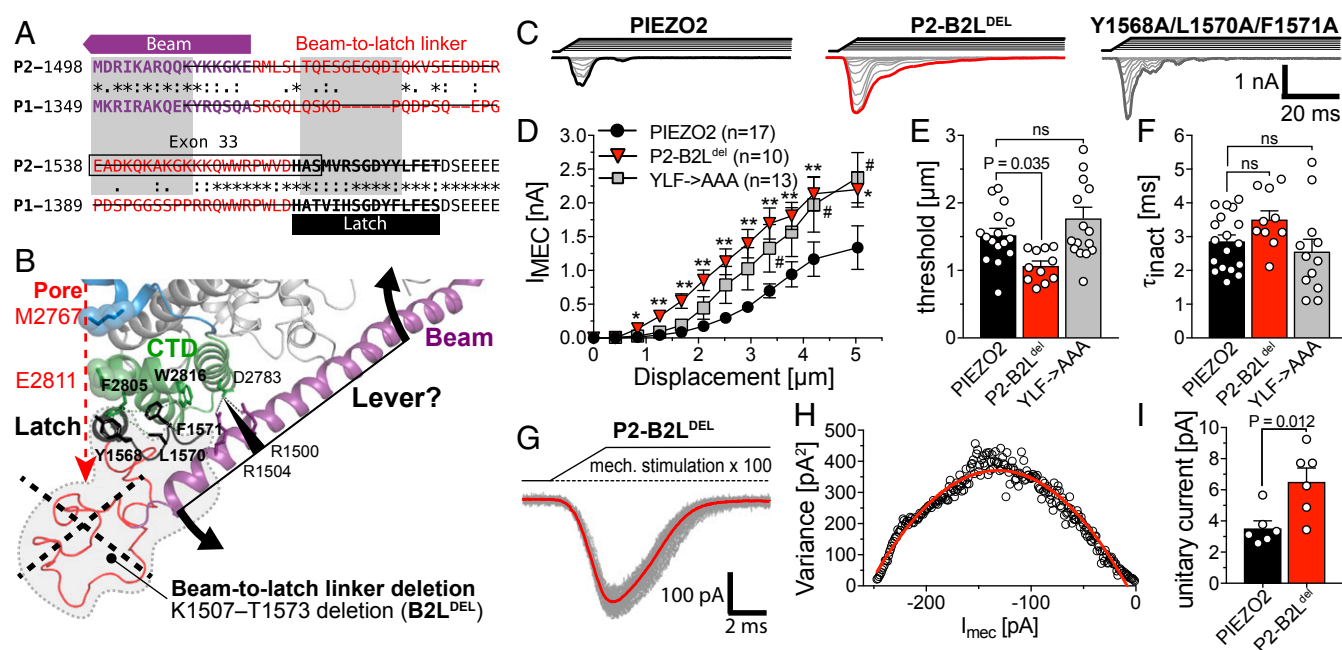

Fig. 3. The beam-to-latch linker limits ion permeation of PIEZO2. (*A*) Sequence alignment of the indicated regions of PIEZO2 and PIEZO1. AAs that were deleted in the B2L^{del} mutants are crossed out. (*B*) Magnified view of the CTD and the proximal end of the beam of a single protamer of the PIEZO2. Note that the beam-to-latch linker region is intrinsically disordered and has not been structurally resolved yet and is thus depicted as an imaginary structure (red line). The gray shaded areas framed by the dashed lines mark the region that was removed in the PIEZO2-B2L^{del} mutant. (*C*) Example traces of PIEZO2-WT (*Left*), PIEZO2-B2L^{del} (*Center*), and YLF→AAA-mediated currents evoked by a series of mechanical stimuli of increasing magnitude in N2a-P1KO cells. (*D*) Displacement–response curves (mean ± SEM peak amplitudes) of the same mutants. The mean current amplitudes at different stimulus strengths were compared using one-way ANOVA and Dunnett's multiple-comparison test. (*E*) Comparison of the mean ± SEM activation thresholds of the mechanically activated currents mediated by the indicated channel mutants using one-way ANOVA and Dunnett's multiple-comparison test. (*F*) Comparison of the mean ± SEM inactivation time constants (τ_{inact}) using one-way ANOVA and Dunnett's multiple comparison test. (*G*) Superimposed example traces (gray) of currents from the PIEZO2-B2L^{del} mutant evoked by 100 consecutive and identical mechanical stimuli. The mean response waveforms obtained by averaging all currents are shown in red. (*H*) The variance of the difference between the measured and the scaled mean waveform at each sampling point is plotted against the current amplitude of the mean scaled waveform in 1-pA bins and fitted using the equation: $\sigma^2 = \sigma_0^2 + iI - I^2/N$, where i is the single-channel current (see *Materials and Methods* and *SI Appendix*, Fig. S3 for details). (*I*) Comparison of the mean unitary currents ± SEM of PIEZO2-WT and B2L^{del} using Student's *t* test.

differences in peak current amplitudes were significant only for some of the tested mechanical stimuli (Fig. 3D) and neither the thresholds nor the inactivation kinetics differed from those of PIEZO2-WT currents (Fig. 3 E and F). Given the partial similarity of the YLF→AAA and the B2L^{del} mutant, we next asked whether AAs other than Y1568/L1570/F1571 are also important. The structure of the last seven C-terminal AAs has also not been resolved, but since they might be located in close proximity to the latch, the B2L-linker, and the proximal end of the beam, they may also be involved in latch–CTD and/or beam–CTD interactions (*SI Appendix*, Fig. S4A). To test this hypothesis, we generated two PIEZO2 mutants in which stretches of three (CTDpolyA1; K2820A/T2821A/N2822A) and four (CTDpolyA2; W2816A/T2817A/R2818A/E2819A) AAs were replaced by alanines. However, both PIEZO2 mutants were fully functional and produced mechanically evoked currents that were indistinguishable from PIEZO2-WT currents (*SI Appendix*, Fig. S4 B–E).

Considering that two recently published studies proposed that PIEZO1 is activated by a lever-like mechanogating mechanism (23, 35), the observation that the PIEZO2-B2L^{del} mutant was fully functional and generated even bigger and more sensitive currents than the PIEZO2-WT channel was completely unexpected and quite surprising. We thus next tested whether the B2L-linker and the latch might have a different function in PIEZO1. To this end we generated a PIEZO1-B2L^{del} mutant that was equivalent to the PIEZO2-B2L^{del} mutant in that it lacks the proximal part of the beam and the beam-to-latch linker as well as the latch domain (Fig. 3A). Strikingly, the PIEZO1-B2L^{del} mutant was also fully functional and, just like the PIEZO2-B2L^{del} mutant, produced significantly larger currents

that inactivated slower than the PIEZO1-WT current, while the reversal potential was not altered (Fig. 4 A–D). Most importantly, cell-attached single-channel recordings PIEZO1-B2L^{del} currents evoked by applying negative pressure via the patch pipette revealed that this mutant, just like the PIEZO2-B2L^{del} mutant, also has an almost two times greater unitary conductance than PIEZO1-WT (Fig. 4 E–G). The single-channel recordings further showed that open probability is not altered in the PIEZO1-B2L^{del} mutant (Fig. 4H).

Hydrophobic Interactions Between Y2807 of the CTD and the Pore-Lining Helices Are Required to Ensure Normal Mechanosensitivity of PIEZO2. Considering that charged residues at the interface between the beam and the CTD are required to ensure normal mechanosensitivity of PIEZO2 (Fig. 2), while the proximal end of the beam appears to be dispensable for channel activation (Fig. 3), we hypothesized that direct interactions between the beam and the CTD facilitate mechanical activation of PIEZO2. We thus next examined the role of the CTD in the mechanogating of PIEZO2. The PIEZO2 homology model suggested that Y2807 located at the proximal end of CTD$^{\alpha2}$ might play an important role as it is located in the center of a hydrophobic pocket formed by the side chains of I2441, H2444, and I2445 protruding from the anchor domain; F2768 of the IH; and M2813 of the CTD$^{\alpha3}$. Importantly, F2768 and M2813 are adjacent to the pore constriction forming AAs M2767 and E2811, respectively (Fig. 5A). Hence, Y2807 appears to be ideally located to allosterically couple conformational changes of the CTD to the channel pore.

To test this hypothesis, we disrupted the putative hydrophobic interaction by substituting Y2807 with the much shorter and less
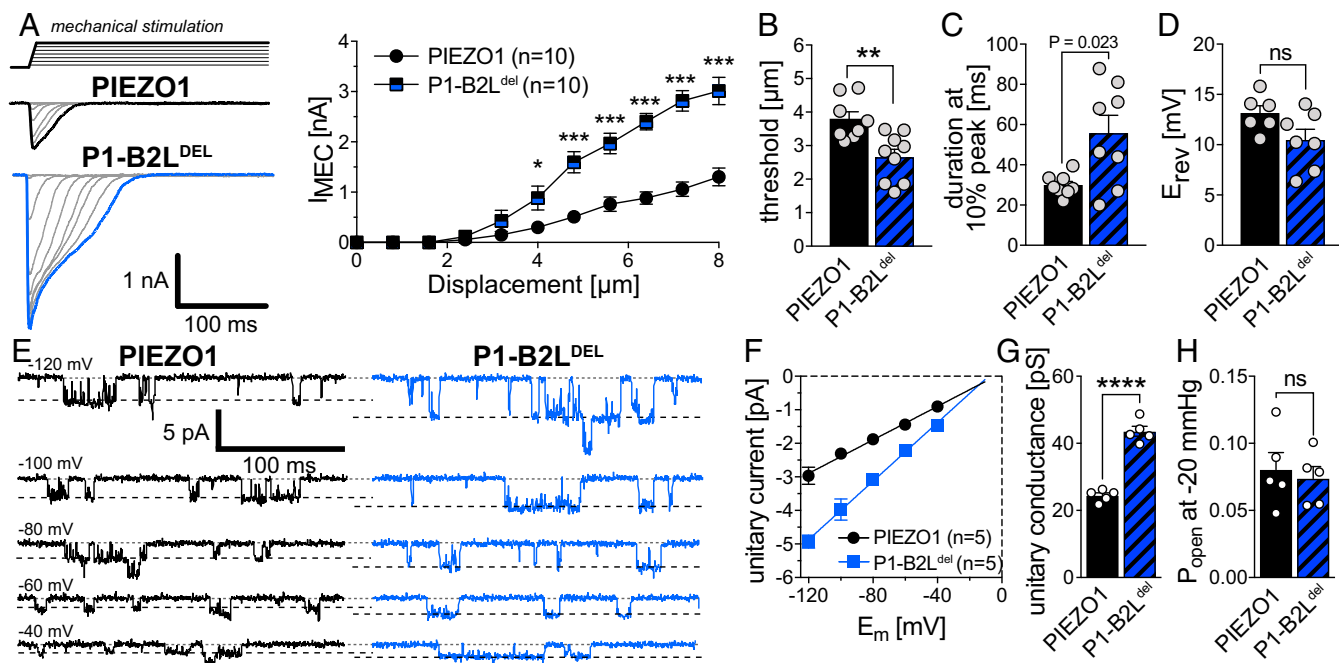

Fig. 4. The beam-to-latch linker limits ion permeation of PIEZO1. (A) Example traces of PIEZO1-WT (*Top Left*) and PIEZO1-B2L^{del} (*Bottom Left*) evoked by a series of mechanical stimuli of increasing magnitude in N2a-P1KO cells and displacement response curves (mean ± SEM peak amplitudes) of the same mutants (*Right*). The mean current amplitudes at different stimulus strengths were compared using Student's t test. (B) Comparison of the mean ± SEM activation thresholds of the mechanically activated currents mediated by the indicated channel mutants using the Mann–Whitney test. (C) Comparison of the mean ± SEM inactivation time constants (τ_{inact}) using Student's t test. (D) Comparison of the mean ± SEM inactivation reversal potential (E$_{rev}$) using Student's t test. (E) Representative traces of stretch-activated channel openings of PIEZO1 (*Left*) and PIEZO1-B2L^{del} (*Right*) elicited application of negative pressure (−20 mmHg) via the patch pipette at the indicated holding potentials. (F) I–V relationship of the stretch-activated channels shown in E. Single-channel amplitudes were determined as the difference between the peaks (Gaussian fits) in the amplitude distribution histogram of the full trace. (G) Comparison of the unitary conductance of PIEZO1 and PIEZO1-B2L^{del} using Student's t test (****P > 0.0001). Conductance was calculated from the slope of linear regression of individual single-channel I–V curves. (H) Comparison of the open probabilities of PIEZO1 and PIEZO1-B2L^{del} using Student's t test.
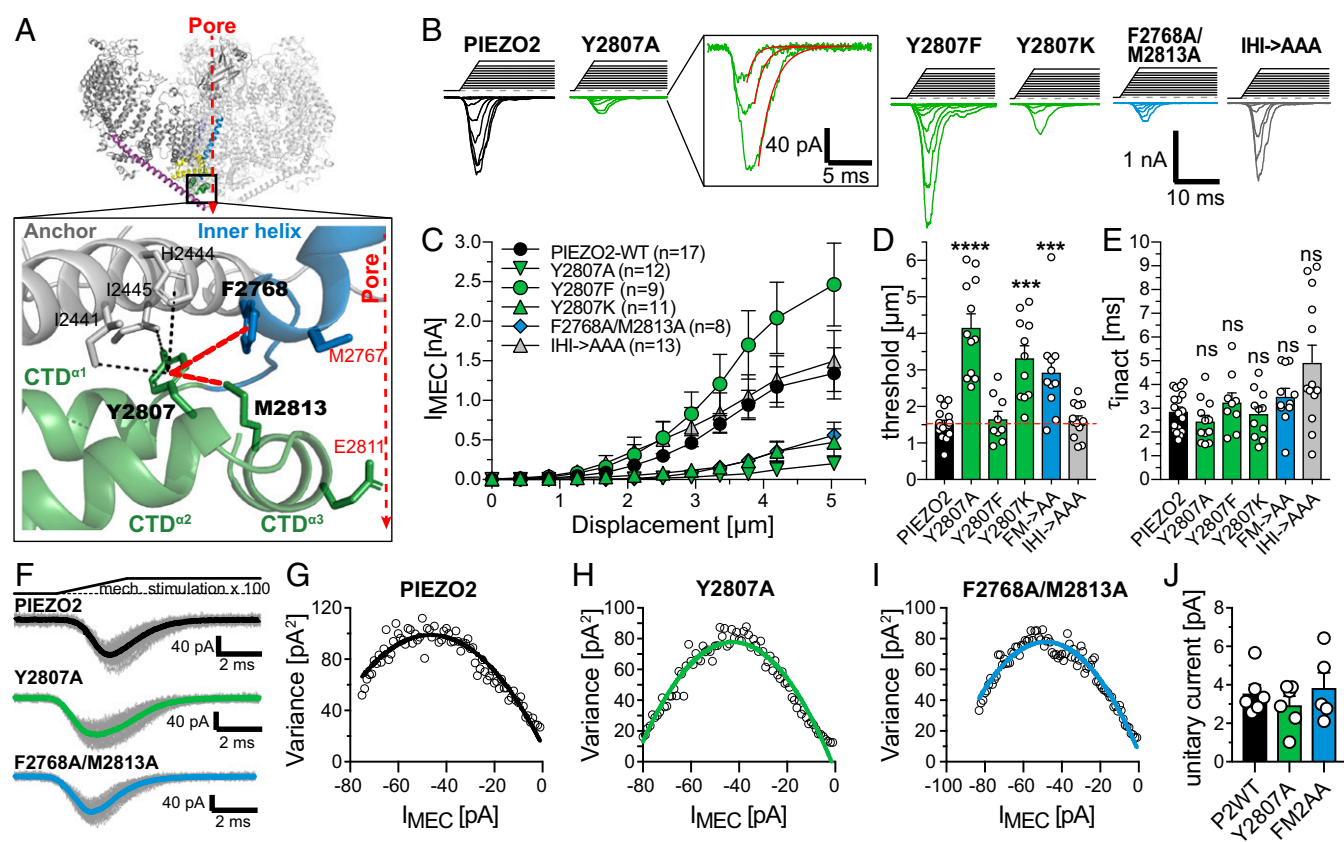
Fig. 5. Interactions between Y2807 of the CTD$^{\alpha 2}$ and the pore-lining helices are crucial for the mechanical activation of PIEZO2. (*A*) Possible hydrophobic interactions of Y2807 with AAs from the Anchor, the IH, and the CTD$^{\alpha 3}$. (*B*) Example traces of mechanically activated currents evoked by increasing mechanical stimuli (*Top*) mediated by the indicated PIEZO2 mutants in N2a-P1KO cells. Note that Y2807A, Y2807K, and F2768A/M2813A mutants generate much smaller currents than PIEZO2-WT, whereas Y2807F generates slightly but not significantly bigger currents. (*C*) Displacement–response curves (mean ± SEM peak current amplitudes) of the indicated PIEZO2 mutants. *N* numbers are shown in the graph. (*D*) Comparison of the mean ± SEM activation thresholds of the mechanically activated currents mediated by the indicated channel mutants using one-way ANOVA with Dunnett's multiple-comparison test. ***P < 0.001, ****P < 0.0001. (*E*) Comparison of the mean ± SEM inactivation time constants (τ_{inact}) using one-way ANOVA with Dunnett's multiple-comparison test. (*F*) Superimposed example traces (gray) of currents from the indicated mutants evoked by 100 consecutive and identical mechanical stimuli. The thick black, green, and blue lines show the mean response waveforms obtained by averaging all currents. (*G–I*) The variance of the difference between the measured and the scaled mean waveform at each sampling point is plotted against the current amplitude of the mean scaled waveform in 1-pA bins and fitted using the equation $\sigma^2 = \sigma_0^2 + iI - I^2/N$, where i is the single-channel current (see *Materials and Methods* and *SI Appendix*, Fig. S2 for details). (*J*) Comparison of the mean single-channel currents ± SEM.

hydrophobic alanine (Y2807A) and assessed the mechanosensitivity of this mutant. Strikingly, the PIEZO2-Y2807A mutant exhibited a significantly greater mechanical activation threshold compared with PIEZO2-WT (Y2807A, 4.16 ± 0.37 μm vs. PIEZO2-WT, 1.53 ± 0.10 μm) and reduced maximum current amplitudes, while inactivation kinetics were not affected (Fig. 5 *B–E*). By contrast, strengthening the putative hydrophobic interaction, by substituting Y2807 with phenylalanine (Y2807F), markedly, although not significantly, increased PIEZO2 peak current amplitudes and did not affect mechanical thresholds (Y2807F, 1.65 ± 0.21 vs. PIEZO2-WT, 1.53 ± 0.10 μm) (Fig. 5 *B–E*) and inactivation kinetics. To test whether the altered mechanosensitivity of the Y2807A mutant resulted from the lower hydrophobicity of alanine compared with tyrosine or resulted solely from the difference in the side chain length, we generated a PIEZO2 mutant in which Y2807 was substituted by lysine (Y2807K), which has a long and positively charged side chain. The Y2807K mutant exhibited the same functional deficits as the Y2807A mutant (Fig. 5 *B–E*).

The Y2807A mutant was properly expressed and trafficked to the cell membrane (*SI Appendix*, Fig. S5 *A–C*) and had similar voltage dependence (*SI Appendix*, Fig. S5 *D and E*) and velocity dependence (*SI Appendix*, Fig. S5F) of activation. Most impor-

tantly, Y2807A exhibited normal unitary current amplitudes (Fig. 5 *F–J*), suggesting that the reduced current amplitudes observed in this mutant result from reduction in mechanosensitivity and the associated right shift in the displacement–response curve. This conclusion is further supported by the observation that in recordings in which very large membrane displacements did not damage the cell or destabilize the gigaseal, the Y2807A mutant exhibited maximal current amplitudes that were in the range of the maximal PIEZO2-WT amplitudes (*SI Appendix*, Fig. S5G). Notably, disrupting the equivalent interaction in PIEZO1 (Y2533A) had the same effect on mechanosensitivity—i.e., significantly smaller currents and higher mechanical thresholds—and did not affect inactivation kinetics and voltage dependence of activation (*SI Appendix*, Fig. S6).

We next asked which of the putative interactions of Y2807 is essential for the normal function of PIEZO2. To this end we substituted F2768 of the IH and M2813 of the CTD$^{\alpha 3}$ as well as I2441, H2444, and I2445 of the anchor domain with alanines (PIEZO2 mutants F2768A/M2813A and I2441A/H2444A/I2445A). The F2768A/M2813A mutant exhibited the same phenotype as the Y2807A mutant—i.e., higher mechanical threshold (F2768A/M2813A, 2.93 ± 0.37 μm vs. PIEZO2-WT, 1.53 ± 0.10 μm) and smaller peak current amplitudes (Fig. 5 *B–D*)—whereas I2441A/H2444A/I2445A-mediated currents were indistinguishable from PIEZO2-WT currents.

In both mutants inactivation kinetics (Fig. 5*E*), membrane expression (*SI Appendix*, Fig. S5 *A–C*), reversal potential (*SI Appendix*, Fig. S5 *D* and *E*), and velocity dependence (*SI Appendix*, Fig. S5*F*) were unaffected. Importantly, nonstationary noise analysis showed that F2768A/M2813A has a similar unitary current amplitude to PIEZO2-WT (Fig. 5 *F–J*). As for the Y2807A mutant, some of the recordings from F2768A/M2813A-expressing cells were stable at high membrane displacements and exhibited large currents in response to these displacements (*SI Appendix*, Fig. S5*H*), which further supported the observation that unitary conductance is not altered in the F2768A/M2813A double mutation.

In summary, our results suggest that hydrophobic interactions between the highly conserved Y2807 and F2768A/M2813A facilitate the mechanical activation of PIEZO2.

Discussion

In this study we set out to investigate the mechanogating mechanism of PIEZO2. Specifically, we examined the role of the beam domain in the mechanical activation of the channel. To address this question, we used site-directed mutagenesis and patch-clamp recordings to identify interdomain interactions that control the mechanosensitivity of PIEZO2.

The Beam Facilitates Mechanical Activation of PIEZO2 but Does Not Seem to Act as a Lever. Our results demonstrate that charged amino acids located at the interface between the beam and CTD facilitate the mechanical activation of PIEZO2 (Fig. 2), whereas the proximal part of the beam as well as the latch domain and the beam-to-latch linker appear to be dispensable for the mechanical activation of the channel (Figs. 3 and 4). Moreover, we show that hydrophobic interactions between the highly conserved Y2807 of the CTD and the pore-lining helices are required to ensure normal mechanosensitivity of PIEZO2 (Fig. 5).

At present we can only speculate about the chemical nature of the interaction between the beam and CTD, but considering that positively charged arginines of the beam (R1500 and R1504) and the negatively charged D2783 of the CTD are involved, it is tempting to hypothesize that these amino acids stabilize the domain interface by forming a salt bridge. Moreover, our mutagenesis experiments do not allow us to draw mechanistic conclusions regarding the role of the beam–CTD interaction in the mechanical activation of PIEZO2. However, since there is evidence suggesting that beam–CTD interactions are also important for the mechanical activation of PIEZO1 (23, 35), it seems likely that this interface has the same function in both channels. For PIEZO1 it has been proposed that the beam acts as a lever, with the distal part serving as the effort arm that moves in response to movements of the blade, the beam–CTD interaction serving as the fulcrum around which the lever rotates, and the proximal part of the beam serving as the load arm of the lever, which opens the channel by pulling on the pore domain, possibly through indirect interactions via the so-called latch domain (23, 35, 40). Experimental evidence for this lever-like mechanogating mechanism has, however, not yet been provided. Our study challenges the lever theory, by showing that the proximal end of the beam—i.e., the putative load arm of the lever—is not required for the mechanical activation of PIEZO1 and PIEZO2 (Figs. 3 and 4). While this observation strongly argues against the previously proposed hypothesis that the beam serves as a lever, it does not definitively rule out the possibility that other channel domains, such as for example the blade domains, might do so.

Considering that none of the loss-of-function mutations that we have identified (Y2807A, F2768A/M2813A, D2738A, and R1500A/R1504A) completely abolished channel function, but solely shifted the mechanical thresholds toward larger membrane indentations (Figs. 2 *C* and *E* and 5 *C* and *D*), we cannot definitively rule out the importance of other interdomain interfaces for the mechanogating of PIEZO2. Thus, it is possible that additional beam-to-CTD interactions, which were not predicted due to the possible inaccuracy of our PIEZO2 homology model, are responsible for the residual mechanosensitivity of the D2783A and R1500A/R1504A mutants (Fig. 2). Moreover, conformational changes in the blade domains might also be transmitted to the pore via interactions with the anchor domain, which is ideally located to transmit blade movements to the CTD and/or the inner helix of the neighboring protamer of the PIEZO2 trimer (Fig. 1*B*). However, previously published studies failed to show an involvement of the anchor domain in mechanogating. Thus, mutations of PIEZO2 E2769 and E2770, which presumably link the anchor to the IH of the same protamer via interactions with H2444 and R2452, as well as the equivalent mutations in PIEZO1, solely affect ion selectivity but not mechanosensitivity of PIEZO1 (29). H2444 is also mutated in our PIEZO2-I2441A/H2444A/I2445A triple mutant, which, consistent with the observations of Zhao *et al.* (29), exhibited normal mechanosensitivity (Fig. 5). Moreover, mutations in PIEZO2-E2416 of the anchor domain and its equivalent E2133 in PIEZO1, which interact with R2756 and R2482, respectively, of the IH of the neighboring protamer, solely affect unitary conductance and Ruthenium Red sensitivity, but not mechanosensitivity of PIEZOs (30). Interestingly PIEZO1-R2482, mutations of which are associated with dehydrated hereditary stomatocytosis in humans (26, 41), has been shown to be involved in voltage modulation of PIEZO1 (20). Finally, mutations in PIEZO1-D2157, which is equivalent to PIEZO2-D2440 that can probably interact with S2760 of the IH of the neighboring subunit, affect neither unitary conductance nor mechanosensitivity (30). Hence, the anchor domain appears to control ion-permeation properties of PIEZO channels and might be required for stabilizing the pore and the trimeric structure (42), but hitherto there is no experimental evidence suggesting that it is also involved in mechanogating of PIEZOs. However, since there are several additional predicted interactions between the anchor and the IH and CTD, which have not yet been investigated, a contribution of the anchor domain to the mechanogating of PIEZOs cannot be definitively ruled out at this point and additional studies will be required to clarify this issue.

The B2L/Latch Domain Controls Ion Permeation of PIEZO2. Single-channel recordings and nonstationary noise analysis of currents mediated by PIEZO1 and PIEZO2 channels lacking the B2L-linker and the latch revealed that these mutant channels have an almost two times greater unitary conductance and accordingly generate exceptionally large mechanically activated whole-cell currents (Figs. 3 and 4). The single-channel recordings further showed that the open probability is not altered in the PIEZO1-B2L^{del} mutant (Fig. 4*H*), suggesting that the B2L/latch region might serve as a cytosolic plug that limits ion permeation.

At present, we can only speculate about the precise mechanism by which this protein region modulates PIEZO function, because its structure has not been resolved for PIEZO1 and, accordingly, is also missing in the PIEZO2 structure homology model. Moreover, several protein disorder prediction tools, such as IUPred, DisEMBL, and VSL2b, suggest that the B2L-linker is intrinsically disordered, which precludes structure modeling of this domain. However, Saotome *et al.* (24) observed a robust density ~4 Å below the lower pore constriction in their PIEZO1 cryo-EM maps, which could not be reliably modeled and which they termed the "cytosolic plug," as it could potentially control ion permeation by blocking the inner vestibule of the ion conduction pathway. Given the close proximity of the B2L-linker to the inner vestibule, it is tempting to speculate that the cytosolic plug is formed by the B2L-linker, which would explain why removing the B2L-linker increases the unitary conductance of PIEZO channels (Figs. 3 and 4). Owing to the lack of structural information it is, however, difficult to predict and test which particular part of the B2L/latch region is responsible for the

modulatory effect and might eventually form the cytosolic plug. Considering that the B2L/latch region appears to have the same function in PIEZO1 and PIEZO2 (Figs. 3 and 4) and considering further that its potential binding site—i.e., the inner vestibule formed by the CTD—is highly conserved between the two channels (∼90% sequence identity), one would assume that binding of the B2L/latch to the CTD would be mediated by an equally conserved region. The only highly conserved region within the B2L/latch domain is a strongly hydrophobic stretch comprising the latch and eight AAs adjacent to the latch (Fig. 3*A*). Considering that a recently discovered splice variant of PIEZO2 that lacks exon 33, which includes the AAs adjacent to the latch (Fig. 3*A*), does not exhibit the same phenotype as the PIEZO2-B2L^{del} mutant (43), it is tempting to speculate that binding of the B2L/latch region to the CTD is mediated by the latch domain. Indeed, changing the hydrophobicity of the latch by substituting three strongly hydrophobic amino acids at the putative interface between the latch and the CTD with alanines (Y1568A/L1570A/F1571A) partially mimicked the effect of the full B2L deletion (Fig. 3 *C–F*), suggesting that binding of the latch to the CTD might be required for bringing the B2L-linker into close proximity of the inner vestibule, such that it can limit ion permeation.

The fact that PIEZOs are not spontaneously active in the absence of the B2L/latch regions shows that there are other gates that keep that channel closed and suggests that the cytosolic plug does not serve as a gating particle. This raises the question of what the function of the cytosolic plug actually is. One possibility is that the cytosolic plug acts as a flow control valve that limits ion permeation by loosely, but not completely, clogging the putative exit of the ion permeation pathway that is located at the center of the inner vestibule, which could explain why removing the cytosolic plug increases the unitary conductance. Another possibility is that the cytosolic plug completely blocks the pore in the closed state and is pulled out from the inner vestibule during the gating process. This, however, seems unlikely, because if the cytosolic plug was really absent from the inner vestibule in the open state, then the unitary conductance would be the same regardless of whether or not the PIEZO has a cytosolic plug, which is not what we observed (Figs. 3*I* and 4*G*). However, another possibility is that the ion permeation pathway of PIEZOs does not extend through the lower constriction, but that the ions actually exit the pore through lateral fenestrations that connect the central canal with the cytoplasm. Indeed such lateral fenestrations have been identified in several ion channels, such as P2X$_3$ or 5-HT$_{3A}$ receptors (44, 45), and have, at least structurally, also been described in PIEZO1 (23, 24). Should the ions exit the pore via these lateral fenestrations, then removing the cytosolic plug would probably open an additional exit from the pore—i.e., the central exit formed by the lower constriction— which could explain why the B2L^{del} mutants have larger unitary conductances. However, to determine whether the lateral fenestrations really represent the ion permeation pathway requires further studies and thus at present we cannot draw a definitive conclusion regarding the mechanism underlying the ion permeation limiting role of the cytosolic plug.

Conclusions

PIEZO2 is the main mechanotransducer in the sensory nervous system and confers mechanosensitivity to proprioceptors (3, 4); to touch receptors (7–9), which also contribute to pain signaling (46, 47); and, as more recently shown, to various types of nociceptors (10, 11). Hitherto, the great majority of our knowledge about the structure–function relationship of PIEZO channels was derived from studies of PIEZO1 and only little was known about PIEZO2. Our study provides important mechanistic insights into the gating mechanism of PIEZO2 and PIEZO1 and thus lays the groundwork for future studies aimed at developing drugs that modulate PIEZO2 function with the ultimate goal being to alleviate pathological pain mediated by touch receptors and nociceptors.

Materials and Methods

Piezo Mutants and Constructs. Mutations were introduced by PCR amplification of Piezo2-IRES-GFP, which was generated by subcloning the IRES-GFP sequence from the pIRES2-EGFP (Clontech/Takara) into a piezo2-pSPORT6 plasmid (gift from A. Patapoutian, Scripps Research Institute, La Jolla, CA), using KAPA HiFi polymerase (Roche) and primers (Sigma Aldrich) containing the selected mutation. For details please see *SI Appendix, Material and Methods*. Piezo2 clones were transformed into Stbl4 electrocompetent bacteria (Invitrogen) to avoid the frequent DNA rearrangements in the Piezo2 ORF. Cells were then grown for 48 h at 30 °C. Piezo1 clones were transformed into DH5α electrocompetent bacteria from NEB and grown for 24 h at 37 °C. For each mutant, several clones were screened for the mutation by sequencing the targeted region and the selected one was entirely sequenced to ensure that no other mutation was present.

Cell Culture and Transfection. N2a-P1KO cells (gift from Gary R. Lewin, Max-Delbrueck-Center for Molecular Medicine, Berlin, Germany) were grown in a 1:1 mixture of Opti-MEM and DMEM supplemented with 10% FBS, 2 mM L-glutamine, and 100 units/mL penicillin streptomycin (all Thermo Fisher) at 37 °C and 5% CO$_2$. For transfection, growth medium was replaced with transfection medium consisting of DMEM, 10% calf serum (Thermo Fisher), and 4 mM L-glutamine and a solution containing 6 μg/mL plasmid DNA, 0.11 mM CaCl$_2$, 25 mM Hepes, 140 mM NaCl, and 0.75 mM Na$_2$HPO$_4$ (pH 7.0) was added. A detailed description of the transfection procedure is provided in *SI Appendix, Material and Methods*.

Patch-Clamp Recordings of PIEZO Currents. Whole-cell patch-clamp recordings were made at room temperature (20–24 °C). Patch pipettes with a tip resistance of 2–5 MΩ were pulled (Flaming-Brown puller; Sutter Instruments) from borosilicate glass capillaries (Sutter Instruments), filled with intracellular solution [125 mM K-gluconate, 7 mM KCl, 1 mM CaCl2, 1 mM MgCl2, 10 mM Hepes, 4 mM EGTA, 2 mM guanosine 5′-triphosphate (GTP), and 2 mM adenosine 5′-triphosphate (ATP) adjusted to pH 7.3 with KOH]. The extracellular solution contained 140 mM NaCl, 4 mM KCl, 2 mM CaCl2, 1 mM MgCl2, 4 mM glucose, and 10 mM Hepes, adjusted to pH 7.4 with NaOH. Recordings were made with an EPC-10 double patch-clamp amplifier (HEKA) in combination with Patchmaster and Fitmaster software (HEKA). Pipette and membrane capacitances were compensated using the autofunction of Patchmaster.

Cells were clamped to a holding potential of –60 mV and stimulated with a series of mechanical stimuli in 0.42-μm increments with a fire-polished glass pipette (tip diameter 2–3 μm) that was positioned at an angle of 45° to the surface of the dish and moved with a velocity of 1 μm/ms by a piezo-driven micromanipulator (Nanomotor MM3A; Kleindiek Nanotechnik). The evoked whole-cell currents were recorded with a sampling frequency of 200 kHz and filtered with a 2.9-kHz low-pass filter. Each cell was stimulated in three different locations and the currents evoked in the most sensitive location were used for analysis. To precisely determine the position in which the mechanical probe first touches the cell—i.e., the starting point of the mechanical stimuli—we used a fire-polished patch pipette that had a small opening at the tip as a mechanical probe, which allowed us to precisely determine the position in which the probe first touches the cell by monitoring the tip resistance with the second head stage of a double patch-clamp amplifier while approaching the cell surface (*SI Appendix*, Fig. S1). This approach ensures that the starting position of the mechanical probe is identical in all recordings and accordingly reduces the variance of the threshold determination as well as the overall error in displacement–response curves of PIEZO2-mediated currents.

The mechanical thresholds of the PIEZO2-mediated currents were determined by measuring the latency between the onset of the mechanical stimulus and the onset of the mechanically activated current. Current onset was defined as the point in which the current signal significantly differed from the baseline current signal ($<I_{mean, baseline} − 6SD_{baseline}$). The membrane displacement at which the current was triggered was then calculated by multiplying the speed at which the mechanical probe moved (1 μm/ms) with the latency. Since the latency of the current onset is independent of current amplitude and is the same for all currents evoked in a given cell (see example traces in Figs. 2–5), this approach is much more reliable and reproducible that other previously used approaches for threshold determination.

The inactivation time constants (τ_{inact}) were measured by fitting the mechanically activated currents with a single exponential function (C1 + C2 × exp(–($t − t_0$)/τ_{inact}),

NEUROSCIENCE

where C1 and C2 are constants, t is time, and τ_{inact} is the inactivation time constant (example fits are shown in Figs. 2D and 5B).

Nonstationary Noise Analysis. To estimate the single-channel current amplitudes of PIEZO2 mutant channels, between 60 and 100 PIEZO-mediated currents were evoked by repeated mechanical stimulation, recorded at 200-kHz sampling frequency, and filtered with an 8-kHz low-pass Bessel filter and the mean response waveform was determined by averaging all recorded currents aligned to the point of current onset—the point where $I_{MEC} = I_{mean}$, baseline – 6·SD$_{baseline}$ (*SI Appendix*, Fig. S2 *B* and *C*). The mean waveform was then scaled to the individual PIEZO-mediated current by setting the peak amplitude of the mean waveform equal to the PIEZO-current amplitude that occurred coincidently with the peak position of the mean waveform (*SI Appendix*, Fig. S2D). The variance of the difference between the measured and the scaled mean waveform at each sampling point was calculated from the isochrones and plotted against the current amplitude of the mean scaled waveform in 1-pA bins. The single-channel current was calculated by fitting the plotted data with the equation $\sigma^2 = \sigma_0^2 + iI – I^2/N$, where σ^2 is the variance, σ_0^2 is the variance at baseline, i is the single-channel current, I is the whole-cell current, and N is the number of channels (*SI Appendix*, Fig. S2E). For a more detailed description of the method please see *SI Appendix*.

Single-Channel Recordings of PIEZO1. Stretch-activated PIEZO1 currents were recorded in the cell-attached patch-clamp configuration using an external solution consisting of 140 mM KCl, 1 mM MgCl$_2$, 10 mM glucose, and 10 mM Hepes adjusted to a pH of 7.3 with KOH. The recording pipettes were coated with Sylgard, had a resistance of 6–8 MΩ, and were filled with a solution containing 130 mM NaCl, 5 mM KCl, 1 mM CaCl$_2$, 1 mM MgCl$_2$, 10 mM TEA-Cl, and 10 mM Hepes adjusted to pH 7.3 with NaOH. Pressure stimuli were applied with a 1-mL syringe and the pressure was measured with a custom-made pressure sensor. Single-channel amplitudes at a given holding potential were determined as the difference between the peaks of Gaussian fits of the trace histograms of five consecutive stimuli using Fitmaster software (HEKA Elektronik GmbH). Unitary conductance was calculated from linear regression fits of the I–V plots of the individual cells. The open probabilities shown in Fig. 4H were calculated by the equation

$$P_{open} = \frac{t_{open}}{(t_{open} + t_{closed})}, \text{ where } t_{open} = \sum_{n=1}^{N} n \cdot t_n \text{ and } t_{closed} = \sum_{n=0}^{N-1} (N-n) \cdot t_n.$$ In the

latter equations N is the total number of channels and t_n is the time for which no channel (t_0), one channel (t_1), two channels (t_2), etc., are open.

Immunostaining and Imaging. Transfected cells were live treated with Wheat Germ Agglutinin–Alexa Fluor 647 conjugate (Life Technologies) by replacing the growth medium with a 5-μg/mL WGA dilution in PBS for 5 min. After 2 PBS washings, cells were fixed with 4% PFA for 10 min, washed three times

for 10 min with PBS (Sigma Aldrich), and permeabilized for 1 h at RT [2% donkey serum (Sigma Aldrich), 1% BSA, 0.1% Triton X-100, 0.05% Tween-20 in PBS]. Samples were then incubated O/N at 4 °C with a 1:2,000 dilution of anti-HA antibody (Sigma-Aldrich; H6908, RRID:AB_260070) in PBS, 1% BSA. After three washes of 10 min, they were incubated for 1 h with a 1:2,000 dilution of AlexaFluor-594 donkey anti-rabbit (Life Technologies; A2107, RRID:AB_141637) and washed three more times. In the second wash, Hoechst 33342 (Thermo Fisher; final concentration 1 μg/μL) was added to stain the cell nucleus.

Confocal images were acquired with an SP8 confocal microscope (Leica) at 1-μm sections. Images shown are the z projection of the acquired image set for each cell.

Biotinylation Assay and Western Blot. To quantify the membrane expression levels of PIEZO2-WT and PIEZO2 mutant channels, we performed a biotinylation assay followed by Western blotting. A detailed description of the procedure is provided in *SI Appendix*.

PIEZO2 Structure Homology Modeling. The PIEZO2 structure homology model was based on the Piezo1 structure (Protein Data Bank code 6B3R) determined at 3.8 Å resolution from Guo and MacKinnon (25). Since the PIEZO1 structure from Guo and MacKinnon (25) did not resolve the latch domain, we generated a second PIEZO2 homology model based on the PIEZO1 structure determined by Saotome *et al.* (24) (6BPZ). The PIEZO2 AA sequence was aligned to PIEZO1 using Clustal Omega (EMBL-EBI), the alignment was uploaded together with the PDB file of the respective structure to the SWISS-MODEL workspace from the Biozentrum (University of Basel), and it was modeled as described by Bordoli *et al.* (36). Except for the regions for which no structure template from PIEZO1 was available (gray shaded areas in Fig. 1A) and which are predicted to be intrinsically disordered, the local QMEAN values indicated a good model quality, especially in the highly conserved Beam, Latch, Anchor, OH, CED, IH, and CTD domains. All molecular visualizations of PIEZO2 were generated with PyMOL 2.0.6.

Statistical Analysis. All statistical analyses were performed in Prism 6.0 (GraphPad). Detailed information about the number of replicates, the statistical tests that were used, and the exact P values is provided in Figs. 1–6.

Data Availability. All PIEZO1 and PIEZO2 mutant constructs are available from the corresponding author upon request.

1. J. Wu, A. H. Lewis, J. Grandl, Touch, tension, and transduction–The function and regulation of piezo ion channels. *Trends Biochem. Sci.* **42**, 57–71 (2017).
2. S. E. Murthy, A. E. Dubin, A. Patapoutian, Piezos thrive under pressure: Mechanically activated ion channels in health and disease. *Nat. Rev. Mol. Cell Biol.* **18**, 771–783 (2017).
3. S.-H. Woo *et al.*, Piezo2 is the principal mechanotransduction channel for proprioception. *Nat. Neurosci.* **18**, 1756–1762 (2015).
4. D. Florez-Paz, K. K. Bali, R. Kuner, A. Gomis, A critical role for Piezo2 channels in the mechanotransduction of mouse proprioceptive neurons. *Sci. Rep.* **6**, 25923 (2016).
5. A. T. Chesler *et al.*, The role of PIEZO2 in human mechanosensation. *N. Engl. J. Med.* **375**, 1355–1364 (2016).
6. S. Maksimovic *et al.*, Epidermal Merkel cells are mechanosensory cells that tune mammalian touch receptors. *Nature* **509**, 617–621 (2014).
7. S. S. Ranade *et al.*, Piezo2 is the major transducer of mechanical forces for touch sensation in mice. *Nature* **516**, 121–125 (2014).
8. K. Schrenk-Siemens *et al.*, PIEZO2 is required for mechanotransduction in human stem cell-derived touch receptors. *Nat. Neurosci.* **18**, 10–16 (2015).
9. S.-H. Woo *et al.*, Piezo2 is required for Merkel-cell mechanotransduction. *Nature* **509**, 622–626 (2014).
10. S. E. Murthy *et al.*, The mechanosensitive ion channel Piezo2 mediates sensitivity to mechanical pain in mice. *Sci. Transl. Med.* **10**, eaat9897 (2018).
11. V. Prato *et al.*, Functional and molecular characterization of mechanoinsensitive "silent" nociceptors. *Cell Rep.* **21**, 3102–3115 (2017).
12. M. W. Kucharczyk *et al.*, Novel mechanisms of bone cancer pain revealed with in vivo GCaMP6s imaging. bioRxiv:10.1101/498980 (17 December 2018).
13. R. Zarychanski *et al.*, Mutations in the mechanotransduction protein PIEZO1 are associated with hereditary xerocytosis. *Blood* **120**, 1908–1915 (2012).
14. B. Coste *et al.*, Gain-of-function mutations in the mechanically activated ion channel PIEZO2 cause a subtype of Distal Arthrogryposis. *Proc. Natl. Acad. Sci. U.S.A.* **110**, 4667–4672 (2013).
15. E. Fotiou *et al.*, Novel mutations in PIEZO1 cause an autosomal recessive generalized lymphatic dysplasia with non-immune hydrops fetalis. *Nat. Commun.* **6**, 8085 (2015).
16. V. Lukacs *et al.*, Impaired PIEZO1 function in patients with a novel autosomal recessive congenital lymphatic dysplasia. *Nat. Commun.* **6**, 8329 (2015).
17. A. A. Mahmud *et al.*, Loss of the proprioception and touch sensation channel PIEZO2 in siblings with a progressive form of contractures. *Clin. Genet.* **91**, 470–475 (2017).
18. M. J. McMillin *et al.*; University of Washington Center for Mendelian Genomics, Mutations in PIEZO2 cause Gordon syndrome, Marden-Walker syndrome, and distal arthrogryposis type 5. *Am. J. Hum. Genet.* **94**, 734–744 (2014).
19. W. Lee *et al.*, Synergy between Piezo1 and Piezo2 channels confers high-strain mechanosensitivity to articular cartilage. *Proc. Natl. Acad. Sci. U.S.A.* **111**, E5114–E5122 (2014).
20. M. Moroni, M. R. Servin-Vences, R. Fleischer, O. Sánchez-Carranza, G. R. Lewin, Voltage gating of mechanosensitive PIEZO channels. *Nat. Commun.* **9**, 1096 (2018).
21. R. Ikeda, J. G. Gu, Piezo2 channel conductance and localization domains in Merkel cells of rat whisker hair follicles. *Neurosci. Lett.* **583**, 210–215 (2014).
22. B. Coste *et al.*, Piezo1 and Piezo2 are essential components of distinct mechanically activated cation channels. *Science* **330**, 55–60 (2010).
23. Q. Zhao *et al.*, Structure and mechanogating mechanism of the Piezo1 channel. *Nature* **554**, 487–492 (2018).
24. K. Saotome *et al.*, Structure of the mechanically activated ion channel Piezo1. *Nature* (2017).
25. Y. R. Guo, R. MacKinnon, Structure-based membrane dome mechanism for Piezo mechanosensitivity. *eLife* **6**, e33660 (2017).
26. C. Bae, R. Gnanasambandam, C. Nicolai, F. Sachs, P. A. Gottlieb, Xerocytosis is caused by mutations that alter the kinetics of the mechanosensitive channel PIEZO1. *Proc. Natl. Acad. Sci. U.S.A.* **110**, E1162–E1168 (2013).
27. W. Zheng, E. O. Gracheva, S. N. Bagriantsev, A hydrophobic gate in the inner pore helix is the major determinant of inactivation in mechanosensitive Piezo channels. *eLife* **8**, e44003 (2019).

28. J. Wu *et al.*, Inactivation of mechanically activated Piezo1 ion channels is determined by the C-terminal extracellular domain and the inner pore helix. *Cell Rep.* **21**, 2357–2366 (2017).
29. Q. Zhao *et al.*, Ion permeation and mechanotransduction mechanisms of mechano-sensitive piezo channels. *Neuron* **89**, 1248–1263 (2016).
30. B. Coste *et al.*, Piezo1 ion channel pore properties are dictated by C-terminal region. *Nat. Commun.* **6**, 7223 (2015).
31. J. Hu, L.-Y. Chiang, M. Koch, G. R. Lewin, Evidence for a protein tether involved in somatic touch. *EMBO J.* **29**, 855–867 (2010).
32. C. D. Cox *et al.*, Removal of the mechanoprotective influence of the cytoskeleton reveals PIEZO1 is gated by bilayer tension. *Nat. Commun.* **7**, 10366 (2016).
33. R. Syeda *et al.*, Piezo1 channels are inherently mechanosensitive. *Cell Rep.* **17**, 1739–1746 (2016).
34. J. Wu, R. Goyal, J. Grandl, Localized force application reveals mechanically sensitive domains of Piezo1. *Nat. Commun.* **7**, 12939 (2016).
35. Y. Wang *et al.*, A lever-like transduction pathway for long-distance chemical- and mechano-gating of the mechanosensitive Piezo1 channel. *Nat. Commun.* **9**, 1300 (2018).
36. L. Bordoli *et al.*, Protein structure homology modeling using SWISS-MODEL work-space. *Nat. Protoc.* **4**, 1–13 (2009).
37. J. Hao, P. Delmas, Recording of mechanosensitive currents using piezoelectrically driven mechanostimulator. *Nat. Protoc.* **6**, 979–990 (2011).
38. S. G. Lechner, H. Frenzel, R. Wang, G. R. Lewin, Developmental waves of mechano-sensitivity acquisition in sensory neuron subtypes during embryonic development. *EMBO J.* **28**, 1479–1491 (2009).
39. S. G. Lechner, G. R. Lewin, Peripheral sensitisation of nociceptors via G-protein-dependent potentiation of mechanotransduction currents. *J. Physiol.* **587**, 3493–3503 (2009).
40. Q. Zhao, H. Zhou, X. Li, B. Xiao, The mechanosensitive Piezo1 channel: A three-bladed propeller-like structure and a lever-like mechanogating mechanism. *FEBS J.* 10.1111/febs.14711 (2018).
41. J. Albuisson *et al.*, Dehydrated hereditary stomatocytosis linked to gain-of-function mutations in mechanically activated PIEZO1 ion channels. *Nat. Commun.* **4**, 1884 (2013).
42. Y. Wang, B. Xiao, The mechanosensitive Piezo1 channel: Structural features and molecular bases underlying its ion permeation and mechanotransduction. *J. Physiol.* **596**, 969–978.
43. M. Szczot *et al.*, Cell-type-specific splicing of Piezo2 regulates mechanotransduction. *Cell Rep.* **21**, 2760–2771 (2017).
44. S. E. Mansoor *et al.*, X-ray structures define human P2X(3) receptor gating cycle and antagonist action. *Nature* **538**, 66–71 (2016).
45. S. Basak, Y. Gicheru, S. Rao, M. S. P. Sansom, S. Chakrapani, Cryo-EM reveals two distinct serotonin-bound conformations of full-length 5-HT$_{3A}$ receptor. *Nature* **563**, 270–274 (2018).
46. R. Dhandapani *et al.*, Control of mechanical pain hypersensitivity in mice through ligand-targeted photoablation of TrkB-positive sensory neurons. *Nat. Commun.* **9**, 1640 (2018).
47. A. Arcourt *et al.*, Touch receptor-derived sensory information alleviates acute pain signaling and fine-tunes nociceptive reflex coordination. *Neuron* **93**, 179–193 (2017).

NEUROSCIENCE